Title	Vortex state and dynamics of a d-wave superconductor: Finite-element analysis
Author(s)	Wang, ZD; Wang, QH
Citation	Physical Review B - Condensed Matter And Materials Physics, 1997, v. 55 n. 17, p. 11756-11765
Issued Date	1997
URL	http://hdl.handle.net/10722/43199
Rights	Creative Commons: Attribution 3.0 Hong Kong License

Vortex state and dynamics of a *d*-wave superconductor: Finite-element analysis

Z. D. Wang
Department of Physics, University of Hong Kong, Pokfulam Road, Hong Kong

Qiang-Hua Wang
Department of Physics, Nanjing University, Nanjing 210093, China
and Department of Physics, University of Hong Kong, Pokfulam Road, Hong Kong

(Received 7 November 1996)

The finite-element method is extended to simulate the *d*-wave time-dependent Ginzburg-Landau equations. By utilizing this method and in the context of the $(s+d)$-wave pairing, we discuss the nature of a single vortex, the structure of equilibrium vortex lattices in bulk samples, the nature of vortices in finite-size samples, and most importantly the transport of the vortices. In particular, the low-field free-flux-flow resistivity turns out to obey the law of corresponding states discovered in conventional superconductors, while the high-field resistivity reveals a noticeable effect of the *s*-wave coupling on lifting the effective upper critical field. The flux flow near and above the depinning current in the presence of a twin boundary or random impurities also assumes a conventional behavior: The current dependence of the flux-flow resistivity can be well described by an overdamped model for a particle subject to driving and pinning forces. However, our results show a noticeable difference between the flux-flow resistivities at large currents in the presence and absence of pinning. [S0163-1829(97)07617-0]

I. INTRODUCTION

The symmetry of the order parameter in high-temperature superconductors appears to be a controversial subject presently. The *d*-wave pairing scenario is strongly supported by evidence for a sign change of the order parameter between the *a* and *b* axes[1] and the observation of a spontaneous half magnetic flux quantum in three-grain-boundary Josephson junctions.[2] However, there are also some observations that are consistent with the *s*-wave pairing instead (with possible anisotropies in the amplitude of the order parameter). For example, a sizable Josephson current in a *c*-axis tunneling junction between Y-Ba-Cu-O (YBCO) and Pb was observed,[3] and *no* angular dependence of the critical current of YBCO-YBCO grain boundary junctions in the *a-b* plane was found.[4] The importance of the pairing symmetry lies in the fact that it is an important probe to the underlying pairing mechanism. On the one hand, a repulsive interaction between electrons can lead to pair formation with *d*-wave symmetry, as in the case where the interaction is suggested to arise from the spin fluctuation exchange.[5] On the other hand, an attractive interaction leads to *s*-wave pairing, with an order parameter without any sign change on the Fermi surface, despite the possible anisotropy in the amplitude. Recently, there have been further efforts[6] by combining the *s*-wave and *d*-wave aspects in order to reconcile the contradictory experimental results.

In another context, given the *d*-wave symmetry of the pairing, it is interesting and important to ask how the macroscopic properties of unconventional superconductors *in the mixed state* would be different from those of conventional superconductors. Volovik may be the first one who studied the density of states of a *d*-wave vortex core.[7] Apart from other consequences of the *d*-wave symmetry, he pointed out that the density of state would scale linearly with $\sqrt{B}$, where B is the magnetic induction. This behavior was observed in a recent specific heat measurement.[8] Soininen *et al.* calculated the vortex structure numerically within the framework of the self-consistent Bogoliubov–de Gennes theory.[9] The detailed structure of a *d*-wave vortex was shown to be very different from that of an *s*- or *p*-wave vortex. Far away from the vortex core a pure *d* wave exists, and near the center there is a normal ''inner core'' where both the *s* wave and *d* wave vanish; in the middle region the two wave components coexist. More interestingly, the *s*-wave component decays as $1/r^2$ and an amplitude profile in a shape of a four-leafed clover arises from both -1 and $+3$ windings. These qualitative features as well as the quantitative details are obtainable from the $d_{x^2-y^2}$-wave Ginzburg-Landau (GL) theory developed by Ren, Xu, and Ting.[10] Numerical simulations[11–13] based on this theory showed that the *d*-wave vortex lattice structure should also be different from the conventional triangular lattice: With increasing temperature the *d*-wave vortex lattice would change from a square lattice to an oblique one and finally to the conventional triangular lattice near the critical temperature. Noticeably, the fact that even a square vortex lattice could be the most stable was also reached by Maki and co-workers[14] from theoretical studies on the quasiparticle spectrum in the vortex state. The numerical as well as theoretical studies provide reasonable interpretation for the experimental results of Keimer *et al.* and Maggio-Aprile *et al.*[15]

In this paper, we are concerned with the effects of the *d*-wave symmetry on the equilibrium as well as the transport properties in the mixed state. We start with the GL equations of a $d_{x^2-y^2}$-wave superconductor,[10] derived on the basis of the microscopic Gor'kov equations.[16] The *effective* interaction between electrons is assumed to be attractive in the *d*-wave channel and repulsive in the *s*-wave channel, so that a uniform superconductor always possesses a pure *d*-wave pairing state. The GL free energy functional for a two-dimensional *d*-wave superconductor can be expressed in terms of two order parameters $S(\mathbf{r})$ and $D(\mathbf{r})$:[10]

$$G=\int d\Omega\ 2\alpha_s|S|^2-\alpha_d|D|^2+\tfrac{4}{3}|S|^4+\tfrac{1}{2}|D|^4+\tfrac{8}{3}|S|^2|D|^2 + \tfrac{2}{3}(S^{*\,2}D^2+\text{H.c.})+2|\mathbf{\Pi}S|^2+|\mathbf{\Pi}D|^2 + (\Pi_x S\Pi_x^* D^*-\Pi_y S\Pi_y^* D^*+\text{H.c.})+(\boldsymbol{\nabla}\times\mathbf{A}-\mathbf{H}_e)^2. \tag{1}$$

Here $\mathbf{\Pi}=i\boldsymbol{\nabla}/\kappa+\mathbf{A}$, with κ being the GL parameter. $\alpha_s=\alpha_{s0}/(1-T/T_c)$ and $\alpha_d=\ln(T_c/T)$, where $\alpha_{s0}=4(1+2V_s/V_d)/N(0)V_d$ is a positive constant with $V_s>0$ $(-V_d<0)$ being the effective interaction strength in the s (d) channel and $N(0)$ being the density of states at the Fermi level. Finally $\mathbf{H}_e$ is the applied magnetic field. Equation (1) is understood to be dimensionless according to the following normalization: The order parameters are normalized by $\Delta_0=\sqrt{4/3\alpha}$ with $\alpha=7\zeta(3)/8(\pi T_c)^2$, the space by the magnetic penetration depth λ, and the vector potential by $\Phi_0/2\pi\xi$ with $\Phi_0=h/2e$ and ξ being the flux quantum and the coherence length, respectively. The time-dependent GL equations pertinent for Eq. (1) can be written as[10]

$$[\eta_s\partial_t+\alpha_s+\tfrac{4}{3}(|S|^2+|D|^2)+\mathbf{\Pi}^2]S+\tfrac{2}{3}D^2S^* + \tfrac{1}{2}(\mathbf{\Pi}_x^2-\mathbf{\Pi}_y^2)D=0, \tag{2}$$

$$[\eta_d\partial_t-\alpha_d+\tfrac{8}{3}|S|^2+|D|^2+\mathbf{\Pi}^2]D+\tfrac{4}{3}S^2D^* + (\mathbf{\Pi}_x^2-\mathbf{\Pi}_y^2)S=0, \tag{3}$$

$$\frac{\partial\mathbf{A}}{\partial t}+\boldsymbol{\nabla}\times\boldsymbol{\nabla}\times\mathbf{A}+\{S^*\mathbf{\Pi}S+\tfrac{1}{2}D^*\mathbf{\Pi}D+\tfrac{1}{2}[S^*(\mathbf{\Pi}_x-\mathbf{\Pi}_y)D + D^*(\mathbf{\Pi}_x-\mathbf{\Pi}_y)S]+\text{H.c.}\}-\boldsymbol{\nabla}\times\mathbf{H}_e=0. \tag{4}$$

Here $\mathbf{\Pi}_k=\hat{x}_k\Pi_k$, and η_s and η_d are two phenomenological constants characterizing the relaxation rate of the s- and d-wave order parameters, respectively. The time t is normalized by $\sigma_n\lambda^2$ with σ_n the normal-state conductivity of the superconductor. We shall take simply $\eta_s=2\,\eta_d=1$ (see, e.g., Ref. 10). In the above equations, we have assumed such a gauge in which the electrostatic potential does not appear. Due to the fully coupled nature among the s wave, the d wave, and the Maxwell equations, rigorous analytical work on the GL equations is extremely difficult or even impossible. Numerical simulations are indispensable in order to achieve a deeper understanding of the d-wave GL theory. Earlier simulations[11] (based on the numerical-relaxation method[17]) are limited to a low GL parameter. However, in a realistic high-T_c superconductor, the GL parameter is rather high. Simulations of the mixed-state high-κ superconductors might become difficult in the context of the usual discretization schemes due to the large ratio between the two relevant length scales ξ and λ. On the other hand, although the relaxation method[17] the authors used in their simulations is well established for the purposes of calculating the equilibrium properties, it has to be extended to simulate the vortex dynamics. Motivated by these considerations, we resort to the d-wave time-dependent GL equations and simulate them by an extension of an earlier method based on the finite-element method.[18] A preliminary announcement was made in an earlier short paper.[13] The present paper, however, is self-containing. It includes a substantially increased understanding of the vortex dynamics in a d-wave superconductor and serves as an important extension of the earlier work. The structure of the rest of the paper is as follows. In Sec. II, we outline the extended finite-element method for our purposes. The application of the method is presented in Sec. III, where we investigate the behavior of vortices in finite-size samples and bulk samples, subject to various types of pinning. The equilibrium as well as the transport properties of the system are discussed. Section IV contains a brief summary of this article.

II. OUTLINE OF THE EXTENDED FINITE-ELEMENT METHOD

The basic idea in the finite-element method (see, e.g., Ref. 19) is to expand, in each element cell of the sample, the functions to be solved by a *complete* set of piecewise shape functions (being unitary at the specified nodal points on the boundary of the cell) and to enforce orthogonality between any of the shape functions and the residual of the governing equations. The latter condition, together with the continuity condition across the element cells and the physical boundary conditions concerned, determines the expansion coefficients and thus the approximate solution. This condition ensures that in the static case the free energy is stationary against any small variations that could also be presumably expanded by the shape functions. The completeness of the shape functions guarantees that the solution converges to the exact solution with decreasing volume of each element. It is clear that in the static situations, the finite-element method, starting with minimizing the free energy in the each element cell, serves as a global minimizer of the total free energy by assembling the elements. In the time-dependent situation, the unknown functions are expanded as the same shape functions but with time-dependent coefficients, which are to be solved by the usual Euler schemes.

As usual, we denote the inner product in the complex Hilbert space by

$$\langle\mathbf{U}|\mathbf{V}\rangle=\int d\Omega\,\mathbf{U}^*\cdot\mathbf{V}, \tag{5}$$

where $\mathbf{U}$ and $\mathbf{V}$ are arbitrary complex scalars or vectors. In an arbitrary element cell, let $\widetilde{S}$, $\widetilde{D}$, and $\widetilde{\mathbf{A}}$ be the shape functions that expand the functions S, D, and $\mathbf{A}$, respectively. The orthogonality condition reads

$$\langle\widetilde{S}|R_s(S,D,\mathbf{A})\rangle=0, \tag{6}$$

$$\langle\widetilde{D}|R_d(S,D,\mathbf{A})\rangle=0, \tag{7}$$

$$\langle\widetilde{\mathbf{A}}|\mathbf{R}_a(S,D,\mathbf{A})\rangle=0, \tag{8}$$

where $R_s(\cdots)$, $R_d(\cdots)$, and $\mathbf{R}_a(\cdots)$ are the residuals, i.e., the left-hand sides of Eqs. (2)–(4) after the substitution of S, D, and $\mathbf{A}$ expanded by the shape functions. After performing integration by parts with respect to the second-order differentials (together with some of the first-order differentials) in $R_{s,d,a}$, we have the weak form of Eqs. (2)–(4), namely, the so-called Galerkin equations:

$$\langle \tilde{S}|\partial_t+\alpha_s+\tfrac{4}{3}(\rho_s+\rho_d)|S\rangle+\langle \tilde{S}|\tfrac{2}{3}D^2S^*\rangle + \langle \mathbf{\Pi}\tilde{S}|\mathbf{\Pi}S+\tfrac{1}{2}(\mathbf{\Pi}_x-\mathbf{\Pi}_y)D\rangle = -\frac{i}{\kappa}\oint \tilde{S}^*\hat{n}\cdot[\mathbf{\Pi}S+\tfrac{1}{2}(\mathbf{\Pi}_x-\mathbf{\Pi}_y)D]dl, \quad (9)$$

$$\langle \tilde{D}|\partial_t-\alpha_d+\tfrac{8}{3}\rho_s+\rho_d|D\rangle+\langle \tilde{D}|\tfrac{4}{3}S^2D^*\rangle + \langle \mathbf{\Pi}\tilde{D}|\mathbf{\Pi}D+(\mathbf{\Pi}_x-\mathbf{\Pi}_y)S\rangle = -\frac{i}{\kappa}\oint \tilde{D}^*\hat{n}\cdot[\mathbf{\Pi}D+(\mathbf{\Pi}_x-\mathbf{\Pi}_y)S]dl, \quad (10)$$

$$\langle \tilde{\mathbf{A}}|\partial_t\mathbf{A}+\{S^*\mathbf{\Pi}S+\tfrac{1}{2}D^*\mathbf{\Pi}D+\tfrac{1}{2}[S^*(\mathbf{\Pi}_x-\mathbf{\Pi}_y)D + D^*(\mathbf{\Pi}_x-\mathbf{\Pi}_y)S]+\text{H.c.}\}\rangle+\langle \nabla\times\tilde{\mathbf{A}}|\nabla\times\mathbf{A}\rangle = \langle \nabla\times\tilde{\mathbf{A}}|\mathbf{H}_e\rangle-\oint \tilde{\mathbf{A}}\cdot[\hat{n}\times(\nabla\times\mathbf{A}-\mathbf{H}_e)]dl, \quad (11)$$

where $\rho_s=|S|^2$, $\rho_d=|D|^2$, and the contour integration of the flux terms is performed over the boundary of the element cell. Here $\hat{n}$ denotes the normal direction of the boundary. Since we enforce continuity of the unknown flux terms across the boundaries between any two adjacent element cells, the contour integrations cancel out after assembling all of the element cells except at the boundary of the sample, where the specific physical boundary conditions are to be substituted (see below). In the following we shall suppress temporarily the flux terms everywhere.

To proceed, we linearize the nonlinear terms in the Galerkin equations using the Newton-Rampson scheme. In particular, for arbitrary functions U, V, and W in the right bracket $|\cdot\rangle$, the product UVW is approximated as

$$UVW\approx U_cV_cW_c+U_cV_c(W-W_c)+U_cW_c(V-V_c)+V_cW_c(U-U_c),$$

where the subscript c denotes the value at the center of the element cell. Decomposing the Galerkin equations in components, we have the element equations written in matrix form:

$$\langle \phi_i|\hat{\sigma}\partial_t+\hat{\mathbf{B}}|\mathbf{\Psi}\rangle=\langle \phi_i|\mathbf{F}\rangle, \quad (12)$$

where ϕ_i is a real piecewise polynomial parent shape function with i being the nodal index; $\mathbf{\Psi}=(S_r,S_i,D_r,D_i,A_x,A_y)^T$ is a six-component vector function representing, respectively, Re(S), Im(S), Re(D), Im(D), A_x, and A_y; $\hat{\sigma}$ is a 6×6 diagonal matrix with $\sigma_{11}=\sigma_{22}=2\sigma_{33,44,55,66}\equiv1$; $\hat{\mathbf{B}}$ is a 6×6 matrix operator with the elements

$$B_{11}=\alpha_s+\frac{1}{\kappa^2}\partial^k\partial_k+A^2+\frac{4}{3}(\rho_s+\rho_d)+\frac{8}{3}S_r^2+\frac{2}{3}(D_r^2-D_i^2),$$

$$B_{12}=\frac{1}{\kappa}(\partial^kA_k-A_k\partial_k)+\frac{8}{3}S_rS_i+\frac{4}{3}D_rD_i,$$

$$B_{13}=\frac{1}{2\kappa^2}(\partial^x\partial_x-\partial^y\partial_y)+\frac{1}{2}(A_x^2-A_y^2)+4S_rD_r+\frac{4}{3}D_iS_i,$$

$$B_{14}=\frac{1}{2\kappa}(\partial^xA_x-A_x\partial_x+A_y\partial_y-\partial^yA_y)+\frac{4}{3}S_rD_i+\frac{4}{3}D_rS_i,$$

$$B_{15}=\frac{1}{\kappa}\left(\partial^xS_i+\frac{1}{2}\partial^xD_i\right)-\frac{1}{\kappa}\left(\partial_xS_i+\frac{1}{2}\partial_xD_i\right)+2S_rA_x+D_rA_x,$$

$$B_{16}=\frac{1}{\kappa}\left(\partial^yS_i-\frac{1}{2}\partial^yD_i\right)-\frac{1}{\kappa}\left(\partial_yS_i-\frac{1}{2}\partial_yD_i\right)+2S_rA_y-D_rA_y,$$

$$B_{22}=\alpha_s+\frac{1}{\kappa^2}\partial^k\partial_k+A^2+\frac{4}{3}(\rho_s+\rho_d)+\frac{8}{3}S_i^2-\frac{2}{3}(D_r^2-D_i^2),$$

$$B_{23}=\frac{1}{2\kappa}(A_x\partial_x-\partial^xA_x+\partial^yA_y-A_y\partial_y)+\frac{4}{3}S_iD_r+\frac{4}{3}S_rD_i,$$

$$B_{24}=\frac{1}{2\kappa^2}(\partial^x\partial_x-\partial^y\partial_y)+\frac{1}{2}(A_x^2-A_y^2)+4S_iD_i+\frac{4}{3}S_rD_r,$$

$$B_{25}=\frac{1}{\kappa}\left(\partial_xS_r+\frac{1}{2}\partial_xD_r\right)-\frac{1}{\kappa}\left(\partial^xS_r+\frac{1}{2}\partial^xD_r\right)+2S_iA_x+D_iA_x,$$

$$B_{26}=\frac{1}{\kappa}\left(\partial_yS_r-\frac{1}{2}\partial_yD_r\right)-\frac{1}{\kappa}\left(\partial^yS_r-\frac{1}{2}\partial^yD_r\right)+2S_iA_y-D_iA_y,$$

$$B_{33}=\frac{1}{2\kappa^2}\partial^k\partial_k-\frac{1}{2}\alpha_d+\frac{1}{2}A^2+\frac{4}{3}\rho_s+\frac{1}{2}\rho_d+D_r^2+\frac{2}{3}(S_r^2-S_i^2),$$

$$B_{34}=\frac{1}{2\kappa}(\partial^kA_k-A_k\partial_k)+D_rD_i+\frac{4}{3}S_rS_i,$$

$$B_{35}=\frac{1}{2\kappa}(\partial^xD_i+\partial^xS_i)-\frac{1}{2\kappa}(\partial_xD_i+\partial_xS_i)+D_rA_x+S_rA_x,$$

$$B_{36}=\frac{1}{2\kappa}(\partial^yD_i-\partial^yS_i)-\frac{1}{2\kappa}(\partial_yD_i-\partial_yS_i)+D_rA_y-S_rA_y$$

$$B_{44}=\frac{1}{2\kappa^2}\partial^k\partial_k-\frac{1}{2}\alpha_d+\frac{1}{2}A^2+\frac{4}{3}\rho_s+\frac{1}{2}\rho_d+D_i^2-\frac{2}{3}(S_r^2-S_i^2),$$

$$B_{45}=\frac{1}{2\kappa}(\partial_xD_r+\partial_xS_r)-\frac{1}{2\kappa}(\partial^xD_r+\partial^xS_r),$$

$$B_{46}=\frac{1}{2\kappa}(\partial_y D_r-\partial_y S_r)-\frac{1}{2\kappa}(\partial^y D_r-\partial^y S_r)+D_i A_y-S_i A_y,$$

$$B_{55}=\frac{1}{2}(\partial^y\partial_y+\epsilon\partial^x\partial_x)+\rho_s+\frac{1}{2}\rho_d+S_r D_r+S_i D_i,$$

$$B_{56}=\frac{1}{2}(-\partial^y\partial_x+\epsilon\partial^x\partial_y),$$

$$B_{66}=\frac{1}{2}(\partial^x\partial_x+\epsilon\partial^y\partial_y)+\rho_s+\frac{1}{2}\rho_d-(S_r D_r+S_i D_i),$$

together with the symmetry $B_{ji}=B_{ij}^{\dagger}$ (defined below); finally, $\mathbf{F}$ is an internal ''force'' operator (arising from the linearization of the nonlinear terms) with the components

$$F_1=\left[\frac{8}{3}(\rho_s+\rho_d)+\frac{4}{3}(D_r^2-D_i^2)+2A^2\right]S_r+\frac{8}{3}D_r D_i S_i+(A_x^2-A_y^2)D_r-\frac{1}{k}(A_k\partial_k-\partial^k A_k)S_i-\frac{1}{2\kappa}(A_x\partial_x-\partial^x A_x+\partial^y A_y-A_y\partial_y)D_i,$$

$$F_2=\left[\frac{8}{3}(\rho_s+\rho_d)-\frac{4}{3}(D_r^2-D_i^2)+2A^2\right]S_i+\frac{8}{3}D_r D_i S_r+(A_x^2-A_y^2)D_i-\frac{1}{\kappa}(\partial^k A_k-A_k\partial_k)S_r-\frac{1}{2\kappa}(\partial^x A_x-A_x\partial_x+A_y\partial_y-\partial^y A_y)D_r,$$

$$F_3=\left[\frac{8}{3}\rho_s+\rho_d+\frac{4}{3}(S_r^2-S_i^2)+A^2\right]D_r+\frac{8}{3}S_r S_i D_i+(A_x^2-A_y^2)S_r-\frac{1}{2\kappa}(A_k\partial_k-\partial^k A_k)D_i-\frac{1}{2\kappa}(A_x\partial_x-\partial^x A_x+\partial^y A_y-A_y\partial_y)S_i,$$

$$F_4=\left[\frac{8}{3}\rho_s+\rho_d-\frac{4}{3}(S_r^2-S_i^2)+A^2\right]D_i+\frac{8}{3}S_r S_i D_r+(A_x^2-A_y^2)S_i-\frac{1}{2\kappa}(\partial^k A_k-A_k\partial_k)D_r-\frac{1}{2\kappa}(\partial^x A_x-A_x\partial_x+A_y\partial_y-\partial^y A_y)S_r,$$

$$F_5=[2\rho_s+\rho_d+2(S_r D_r+S_i D_i)]A_x+\frac{1}{\kappa}(S_i\partial_x S_r-S_r\partial_x S_i)+\frac{1}{2\kappa}(D_i\partial_x D_r-D_r\partial_x D_i)+\frac{1}{2\kappa}(S_i\partial_x D_r+D_i\partial_x S_r-S_r\partial_x D_i-D_r\partial_x S_i)-\frac{1}{2}\partial^y H_e+\frac{1}{2}J_x,$$

$$F_6=[2\rho_s+\rho_d-2(S_r D_r+S_i D_i)]A_y+\frac{1}{\kappa}(S_i\partial_y S_r-S_r\partial_y S_i)+\frac{1}{2\kappa}(D_i\partial_y D_r-D_r\partial_y D_i)-\frac{1}{2\kappa}(S_i\partial_y D_r+D_i\partial_y S_r-S_r\partial_y D_i-D_r\partial_y S_i)+\frac{1}{2}\partial^y H_e+\frac{1}{2}J_y.$$

In the above equations, a repeated index k implies summation over the x,y components, ∂^k and ∂_k denote partial derivative operators acting on the left-hand and right-hand *nearest-neighbor* functions, respectively, $B_{ij}^{\dagger}$ is the same as B_{ij} except that the operators ∂^k and ∂_k are exchanged. In obtaining B_{ij} and F_i, we have multiplied Eqs. (3) and (4) by a factor of 1/2 in order to make the resulting matrix $\hat{\mathbf{B}}$ apparently conjugate. We have dropped, for simplicity, the subscript c for all of the functions in B_{ij} and F_i defined at the center of the element cell, which are understood to be the (time-dependent) properties of the cell. (Note that some of the properties are derivatives at the cell center.) The ϵ terms in B_{ij} arise from the penalty functional $\epsilon(\nabla\cdot\mathbf{A})^2$ ($\epsilon>0$), which is inserted into the integrand of Eq. (1) to enforce the London gauge $\nabla\cdot\mathbf{A}=0$.[18] (In the case of periodic boundary conditions in both x and y directions, the H_e terms and ϵ terms can be ignored.) Moreover, we have assumed that $\mathbf{H}_e=H_e\hat{z}$ is uniform over the sample and that a transport current $\mathbf{J}=J_x\hat{x}+J_y\hat{y}$ is applied.

The function $\mathbf{\Psi}$ can be expanded in an element cell by the real parent shape functions ϕ_i as follows:

$$\mathbf{\Psi}=\sum_i \mathbf{Q}_i\phi_i, \tag{13}$$

where $\mathbf{Q}_i$ is a (time-dependent) coefficient vector. After completing the integration over each element cell in Eq. (12) and assembling all of the resulting element equations, we obtain a set of ordinary differential equations, which can be formally written as

$$(\hat{C}\partial_t+\hat{K})\vec{a}=\vec{f}, \tag{14}$$

where $\hat{C}$ and $\hat{K}$ are usually referred to as the capacity matrix and stiffness matrix, respectively, $\vec{a}$ is the global coefficient vector, and $\vec{f}$ is the assembled force vector. The semidiscretized equation (14) can be further discretized in time by the usual implicit or explicit (backward or forward) Euler methods. The implicit scheme discretizes Eq. (14) at the $(n+1)$th time step into

$$\left(\frac{1}{\Delta t}\hat{C}+\hat{K}\right)\vec{a}_{n+1}=\vec{f}-\frac{1}{\Delta t}\hat{C}\vec{a}_n, \tag{15}$$

which behaves as an overdamped system, converges absolutely for an arbitrary time step Δt (>0) in the case of linear evolution equations,[19] and also proves to be extremely stable in our (nonlinear) case (even if $\Delta t\sim 10$). This is a desirable feature if the system relaxes with a very long time scale. However, the implicit scheme could be rather time-consuming since the effective stiffness matrix $\hat{K}_{\rm eff}=(1/\Delta t)\hat{C}+\hat{K}$ has to be inverted at each time step (due

to the time dependence of $\hat{K}$). In the case of periodic boundary conditions the problem is more severe since the relevant matrix $\hat{K}_{\rm eff}$ is not banded at all and the usual matrix inversion scheme for banded matrices ceases to be efficient. In the explicit scheme, on the other hand, Eq. (14) is further discretized in time into

$$\frac{1}{\Delta t}\hat{C}\vec{a}_{n+1}=\vec{f}-\left(\frac{1}{\Delta t}\hat{C}+\hat{K}\right)\vec{a}_n, \tag{16}$$

where the effective stiffness matrix $(1/\Delta t)\hat{C}$ is constant and can be diagonalized trivially once and forever using the well-known lumping method (see, e.g., Ref. 19). Thus the explicit scheme could be desirable for large systems (irrespectively of the boundary conditions). Unfortunately, the explicit scheme converges conditionally at very small $\Delta t \leqslant \Delta t_{\max}$ (which could be determined from the extremum eigenvalues of the governing iteration equations). See Ref. 19 for more details on the assembling of the element equations and the comparison between implicit and explicit Euler schemes.

In closing this section, we give a brief description for the implementation of the boundary conditions in a variety of situations. There are two kinds of boundary conditions concerned. The first is the so-called natural boundary condition, which can be directly submitted into the force terms of the assembled Galerkin equations. Examples of natural boundary conditions are

$$\hat{n}\cdot[\mathbf{\Pi}S+\tfrac{1}{2}(\mathbf{\Pi}_x-\mathbf{\Pi}_y)D]_\Gamma=0, \tag{17}$$

$$\hat{n}\cdot[\mathbf{\Pi}D+(\mathbf{\Pi}_x-\mathbf{\Pi}_y)S]_\Gamma=0, \tag{18}$$

$$\hat{n}\times(\nabla\times\mathbf{A}-\mathbf{H}_e)|_\Gamma=0, \tag{19}$$

where Γ represents the sample boundary. Equations (17) and (18) guarantee that the supercurrent does not flow out of the sample, and Eq. (19) is the usual boundary condition for the magnetic field. The second is the so-called essential boundary condition, which prescribes the function values on the boundary. The periodic boundary conditions fall into this category. The degrees of freedom prescribed by the essential boundary conditions are eliminated *prior* to calling a solver for the governing equations. In addition, in the presence of a twin boundary, the properties of the system may change sharply across the boundary. For example,

$$\alpha_{s,d}=\alpha_{s0,d0}+V_{s,d}\delta(y-y_0) \tag{20}$$

describes the variation of $\alpha_{s,d}$ across the twin boundary along the line $y=y_0$. This property can also be incorporated naturally into the Galerkin equations as if the twin boundary were an extra boundary of the sample, with the discontinuity conditions

$$\frac{i}{\kappa}\hat{n}\cdot[\mathbf{\Pi}S+\tfrac{1}{2}(\mathbf{\Pi}_x-\mathbf{\Pi}_y)D]_-^+=-V_sS, \tag{21}$$

$$\frac{i}{\kappa}\hat{n}\cdot[\mathbf{\Pi}D+(\mathbf{\Pi}_x-\mathbf{\Pi}_y)S]_-^+=-V_dD, \tag{22}$$

which follow immediately from an integration of Eqs. (2) and (3) along the normal direction $\hat{n}$ of the twin boundary over an infinitesimal interval. Here $[\,\cdot\,]_-^+$ means the jump of the argument across the boundary. Note that when there are misorientations across the twin boundary or when the a and b axes of the superconducting crystalline are not aligned with the operating frame, transformations with respect to the spatial derivatives should be performed in the Galerkin equations according to the operating frame.

III. EQUILIBRIUM AND TRANSPORT BEHAVIORS OF VORTICES

A. Vortex structure

For the d-wave superconductors, the equilibrium vortices and vortex structures have been studied recently,[11,12] while neither vortices in finite-size samples nor transport behaviors of vortices have been examined with the GL equations. For finite-size samples the difficulty might lie in the implementation of the natural boundary conditions in the usual finite-difference method. However, as discussed in the previous section, the boundary conditions can be implemented with great ease in the present finite-element method. Another feature of the latter method is a smooth and steady convergence. In this section, the vortices in both bulk and finite-size samples are examined. Some of the results have been presented in a recent publication[13] and will be mentioned only briefly in this paper.

In Ref. 13, we found excellent agreement between the results obtained by the finite-element method and by the relaxation method[11] regarding the static single-vortex profile. In particular, the fourfold symmetry as seen from the plots of the s- and d-wave amplitudes was reproduced. Moreover, we have also simulated the vortex lattice for values of κ up to 10, at which level the simulation by the usual algorithm becomes not efficient enough. By using the implicit Euler scheme for the time evolution of the coefficients in the finite-element method, the iteration time step could be varied fairly arbitrarily up to $\Delta t=100$, and the iteration would converge after only tens to hundreds of iteration steps with Δt being of order 10. Therefore, we can safely reach the steady-state solution of the GL equation and thus give reliable results regarding the equilibrium properties. For a fixed area of the unit cell, we have obtained steady-state solutions as a function of the lattice structure represented by the side-length ratio r at various s-wave channel parameter α_s (not plotted here). In a realistic sample, the equilibrium vortex structure corresponds to the optimal value of r that minimizes the free energy. Our results showed that with increasing temperature (or α_s) the vortex lattice would change from a square to a triangular structure, a phenomenon in agreement with earlier simulations,[11,12] predictions,[14] and seemingly some experiments.[15] This effect has been ascribed to the fourfold symmetry of the system: Restoring of the fourfold symmetry lowers the potential energy while lifting the kinetic energy and the field energy. With increasing α_s (or increasing temperature below and near T_c), the s-wave component is suppressed and plays less of a role. Near T_c, the system is well described by the single order parameter D, being equivalent to a conventional isotropic system.

Figure 1 shows the amplitudes of the s-wave and d-wave component order parameters at $\kappa=10$ and

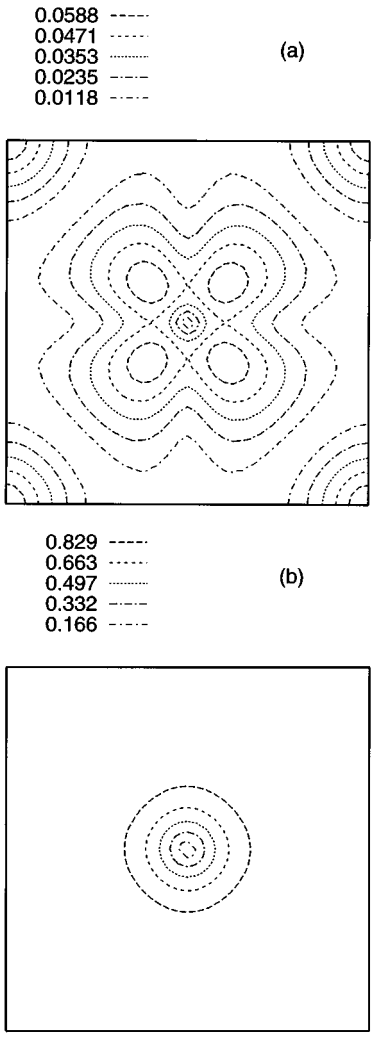

FIG. 1. Contour plot of the order parameters in an open boundary, $\kappa=10$, $10\xi\times10\xi$ sample under an applied field of $H_e=1.5$. (a) The *s*-wave amplitude, (b) the *d*-wave amplitude.

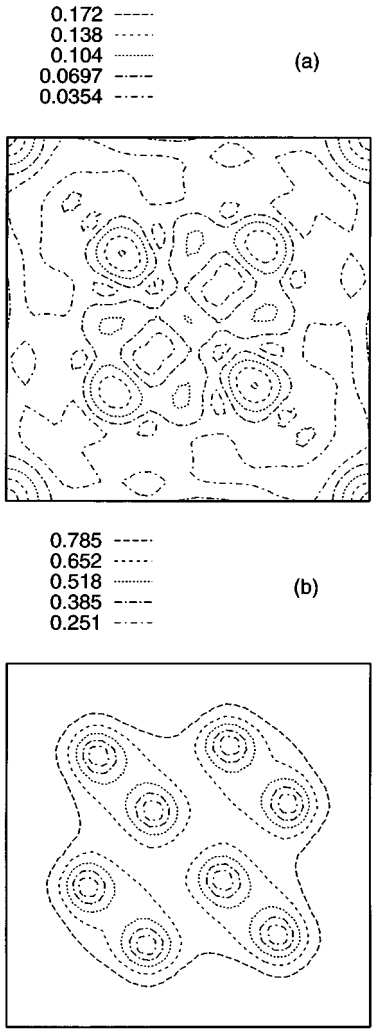

FIG. 2. Contour plot of the order parameters in an open boundary, $\kappa=6$, $11.4\xi\times11.4\xi$ sample under an applied field of $H_e=4$. (a) The *s*-wave amplitude, (b) the *d*-wave amplitude.

$\alpha_s=\alpha_d=1$ in an open boundary $10\xi\times10\xi$ square sample under an applied field of $H_e=1.5$. A single vortex has penetrated the sample. While the *d*-wave amplitude in Fig. 1(b) is flat at the boundaries, the *s*-wave amplitude is enhanced at the four corners of the sample. This is different from the case of a dilute vortex lattice in a bulk sample, where the *s*-wave component is only enhanced around the vortex core.[11,13] Figure 2 is the same as Fig. 1 but in a $11.4\xi\times11.4\xi$ square sample with $\kappa=6$ and $H_e=4$. Eight vortices have penetrated into the sample. We see the same corner effect as in Fig. 1. Moreover, the eight vortices have arranged themselves in such a way as to form almost a square lattice, being consistent with the bulk property discussed above.

B. Free vortex flow

In Ref. 13 we have also considered the evolution of the vortices in a tapelike sample under an applied current along the longitudinal direction of the tape. The vortices penetrate from the right boundary, move in the direction of the Lorentz force in the interior, and annihilate at the left boundary. The *s*-wave component of the order parameter is seen to ride over the *d*-wave component adiabatically. It should be pointed out that the algorithm described in the previous section applies best for relaxation problems with no applied current, while in the presence of an applied current the vector potential would increase endlessly in the fixed gauge (in the absence of an electrostatic potential), and one would soon lose accuracy in the iteration. The heuristic reason is as follows. A large amplitude of the vector potential amounts to a large gradient in the phase φ (and thus in the real and imaginary parts) of the order parameter so as to keep the physically meaningful gauge-invariant phase $\varphi-\kappa\int\mathbf{A}\cdot d\mathbf{r}$ varying slowly in space. This requires a smaller and smaller element cellular volume to approximate accurately violent spatial variations of the relevant functions when the average vector potential $\mathbf{A}_0=\langle\mathbf{A}\rangle$ becomes large. But we are using a fixed volume of the element cells. To get around this problem, we have performed global gauge transformations after each step of iteration,

$$\mathbf{A}\rightarrow\mathbf{A}-\mathbf{A}_0,\quad \varphi\rightarrow\varphi-\kappa\int\mathbf{A}_0\cdot d\mathbf{r}, \tag{23}$$

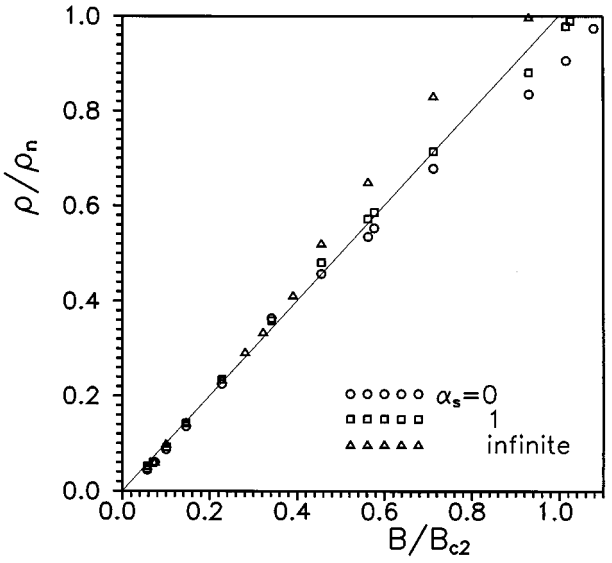

FIG. 3. Magnetic field dependence of the free-flux-flow resistivity at various values of α_s. The solid line represents the conventional law of corresponding states.

which is justified for adiabatic dynamics, e.g., when the applied current is significantly lower than the depairing current J_{c0} (Ref. 20), so that the vortices can move steadily. (It should be pointed out that the periodic boundary condition for the phase φ should be twisted accordingly.) In this case, the instant spatial average of the electric field is simply given by $\mathbf{E}=\mathbf{A}_0/\Delta t$. Therefore, the transport behavior of the system can be simulated without difficulty. The above modification for the dynamic case applies equally well in open boundary problems and periodic boundary problems.

Since the boundary plays an important role in finite-size samples, we would rather study the vortex transport using periodic boundary condition in order to mimic the bulk properties. We use a square unit cell of grid size $L_x \times L_y = 19 \times 19$, threaded by one or two vortices. The side length is varied so as to change the magnetic induction B. The GL parameter is set to be $\kappa=3$. Figure 3 shows the B dependence of the free-flux-flow (FFF) resistivity for $\alpha_s=0$ (diamonds), $\alpha_s=1$ (crosses), and $\alpha_s=\infty$, respectively. In all the cases we fixed $\alpha_d=1$. This is applicable since we can always rescale the order parameters and relevant variables. Recalling the temperature dependence of the original α_s and α_d described in Sec. I, we notice that these values of α_s correspond to, respectively, an extremely low temperature, a temperature of roughly $(0.7–0.9)T_c$, and a temperature in the immediate vicinity of the critical temperature. In all cases we used a driving current $J_x=0.1$. The current-voltage characteristics are linear at this level of current except for fields close to the bare upper critical field $B_{c2}=\Phi_0/2\pi\xi^2$. The resistivity in Fig. 3 seems to be linear in B at low fields. It is thus interesting to note that although the thermal capacity of a d-wave superconductor might vary as $\sqrt{B}$ due to the same dependence in the quasiparticle spectrum,[14,7] the FFF resistivity seems to assume a behavior similar to that in a conventional s-wave superconductor, i.e., the law of corresponding states ($\rho/\rho_n \propto B/B_{c2}$).[21] However, the B dependence of the resistivity begins to deviate from the linear law at $B \geqslant 0.5B_{c2}$. The data for different α_s at fixed field are scattered in a fashion with the magnitude of the (reduced) resistivity increasing with α_s. Moreover, the data curve for $\alpha_s=0$ is bent downward at $B \sim B_{c2}$, suggesting that enhancement of the s wave (at decreasing temperature) should stabilize the vortex state. Defining an effective upper critical field $\tilde{B}_{c2}$ as the field at which the flux-flow resistivity reaches the normal state resistivity, we see clearly from Fig. 3 that $\tilde{B}_{c2} > B_{c2}$ for $\alpha_s=0$. The nonlinearity at $B \geqslant 0.5B_{c2}$ for $\alpha_s=\infty$ may arise from the nonlinearity in the current-voltage characteristics around $J=0.1$. Another aspect may be the boundary condition we have applied, which is in principle inaccurate for $\alpha_s=\infty$ and at $B \sim B_{c2}$ where the vortices would be densely distributed as a *triangular* lattice in equilibrium (instead of a square lattice we have used at the outset).

C. Effects of twin boundaries

Next, we examine the effects of a twin boundary on the vortices. To be clear off the sample boundary, we use again the periodic boundary condition with one flux quantum in a $3.5\lambda \times 3.5\lambda$ unit cell for $\kappa=3$. We also apply a transport current J in the x direction, in parallel to the periodic arrays of twin boundaries (with a transverse spacing of $L=3.5\lambda$) described by $\alpha_i=\alpha_{i,0}+V_i\Sigma_k\delta(y-kL)$, where the subscript i stands for s or d. Here we assume that the twin boundaries are created by some chemical method in a parent crystal with no misorientations. Otherwise, two twin boundaries are needed in one unit cell to apply the periodic boundary condition. In Figs. 4 and 5, $\alpha_{s,0}=\alpha_{d,0}=1$, $V_s=0.1$, and $V_d=-0.5$. (In fact, V_s is irrelevant as long as $\alpha_s>0$.) Figures 4(a), 4(b), and 4(c) are contour plots of the s-wave amplitude, d-wave amplitude, and the field distribution, respectively, at $J=J_x=0.1$. Along the twin boundary, the d-wave order parameter is suppressed while the s-wave order parameter is greatly enhanced. Due to the applied transport current, the vortex profile is displaced by the Lorentz force (in the y direction). However, the vortex remains to be pinned at the twin boundary up to $J_x=0.14$ when the vortex begins to move. On the other hand, as compared to the case in the absence of the twin boundaries, the order parameter profiles are deformed significantly, while the field profile is only slightly changed into an ellipselike shape. This is an immediate consequence of the two well-defined length scales ξ and λ. A similar phenomenon has been observed in s-wave superconductors.[22] Figure 5(a) shows the evolution of the spatially averaged electric field E at $J=0.14$ (diamonds) and $J=0.2$ (crosses), respectively. Evidently, the twin boundary modulates the vortex motion. The resistivity is obtained from $\rho/\rho_n=\langle E\rangle_t/J$ where the average over time is performed. Figure 5(b) shows the current dependence of the flux-flow resistivity. In contrast to the FFF resistivity, the flux-flow resistivity in the presence of pinning is highly nonlinear in the applied current. Since we have not included the thermal noise in the simulations, we expect that $\rho/\rho_n=a\sqrt{1-(J_c/J)^2}$ at $J \geqslant J_c$, where a is the asymptotic reduced resistivity and J_c is the depinning current (to be determined), in a similar fashion to the case of a sinusoidal pinning potential in a more phenomenological overdamped model: $\eta\dot{X}=F_L+F_p(X)$ with F_L as the Lorentz force and

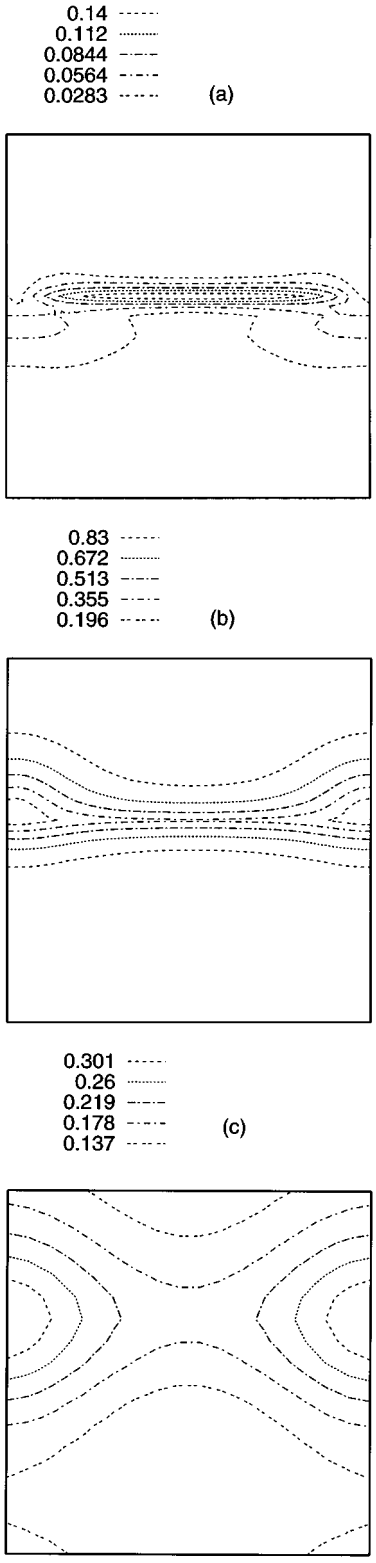

FIG. 4. Contour plots of (a) the *s*-wave amplitude, (b) the *d*-wave amplitude, and (c) the field distribution for a vortex in a unit cell with a twin boundary. See the text for details.

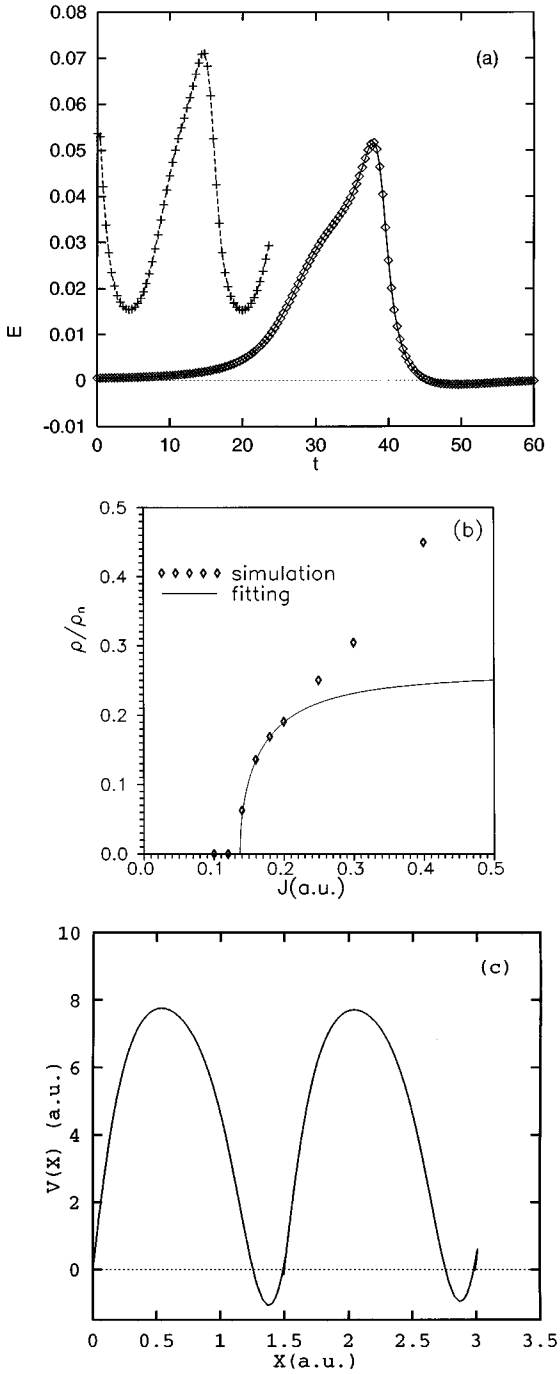

FIG. 5. (a) The time dependence of E at $J=0.14$ (diamonds) and $J=0.2$ (crosses), respectively. (b) The current dependence of the flux-flow resistivity. The solid line represents a fitting at low J. (c) The pinning potential profile extracted from (a) for $J=0.14$.

F_p as the spatially periodic pinning force. The fitting for the J dependence of ρ in the vicinity of the depinning current in Fig. 5(b) indicates indeed such a behavior and gives $a=0.26$ and $J_c=0.137$. To bear out the pinning potential in our case, we could perform an average of E over $X\propto\int E dt$ (*instead of* over t) and subtract by this average from the X dependence of E to find the X dependence of the pinning force $F_p(X)$, and hence the pinning potential $V(X)=-\int F_p(X)dX$. Figure 5(c) is obtained in such a way for $J=0.14$. The pinning potential profile around each dip mimics the standard result $V(X)\sim -K_0[2(X-X_0)]+\text{const}$ [with X being in units of λ and $K_0(\cdot)$ the zeroth-order Bessel function].[23] This indicates that the overdamped particle model still works well in the *d*-wave superconductor at this level of applied current. However, with increasing J, the

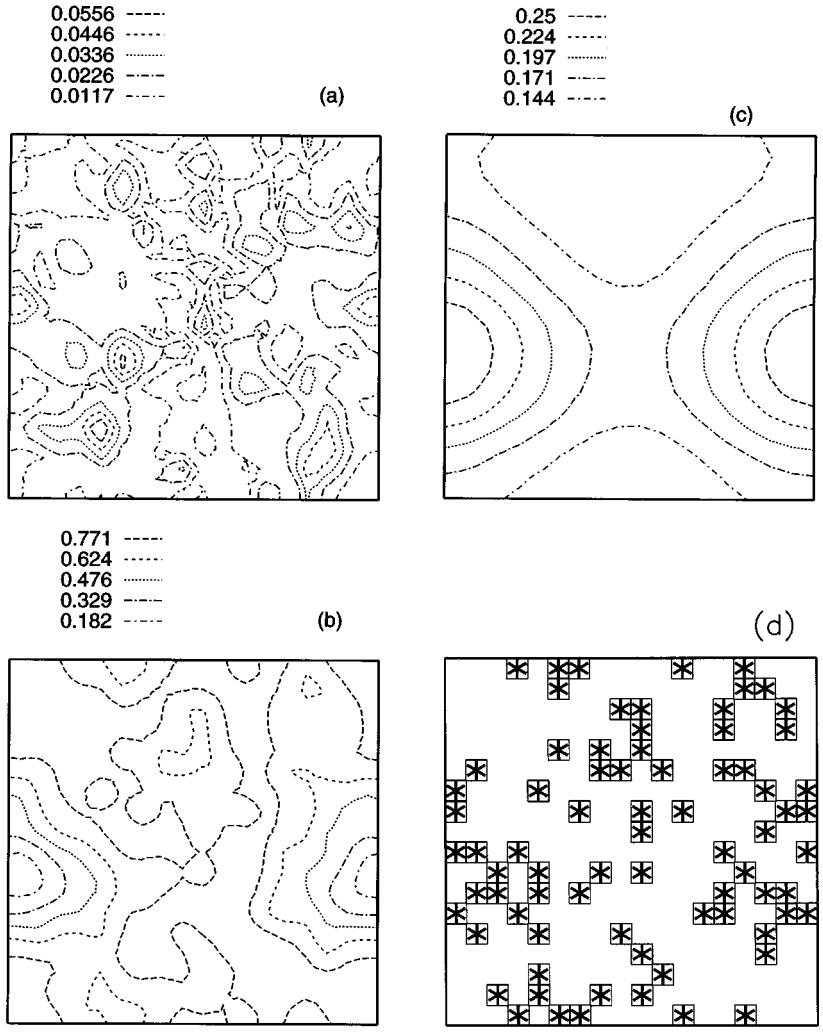

FIG. 6. Contour plots of (a) the *s* wave, (b) the *d* wave, and (c) the local magnetic field. (d) is a schematic plot of the location of the impurities (bold stars).

resistivity increases violently, as is understandable since the applied current is reaching the depairing current $J_{c0}=0.3849$.[20] Moreover, the asymptotic resistivity in the fitting curve of Fig. 5(b), $0.26\rho_n$, is already significantly larger than the corresponding resistivity $\sim 0.05\rho_n$ in Fig. 3. Therefore, the presence of a twin boundary pins the vortex at low J, on the one hand, and increases the asymptotic resistivity at large J, on the other hand, presumably because the twin boundary lowers the superfluid density from the viewpoint of the two-fluid model. The latter fact is often ignored tacitly in the overdamped model. Our finding suggests that caution should be taken in the application of the overdamped model in which the asymptotic resistivity is assumed to be the corresponding FFF resistivity in disorder-free superconductors.

D. Effects of disorders

Figures 6(a)–6(c) are, respectively, contour plots of the *s* wave, the *d* wave, and the field of a vortex in a unit cell of the same size and with the same κ as in Fig. 4, but with some randomly distributed pointlike impurities, schematically shown in Fig. 6(d) as bold stars. $\alpha_d=-1$ in the impurity cells while $\alpha_d=1$ elsewhere. Each impurity cell has dimensions $1.2\xi\times 1.2\xi$ in space. The occupation of the impurities is $p=0.2$. From Fig. 6, we see that the order parameters are modulated by the disorders, which break the fourfold symmetry, while the field profile is hardly distorted. This is similar to the case of a twin boundary mentioned in the previous section. Moreover, the *d*-wave amplitude is slightly suppressed by the impurities, while the *s*-wave amplitude is enhanced at the interfaces between the impurity sites (with $\alpha_d=-1$) and the superconducting area (with $\alpha_d=1$). Due to the long-range coherence of the order parameter, however, the *d* wave retains an appreciable amplitude above zero except in the vortex core, and varies in space rather smoothly, irrespective of the sharp change of α_d at the impurity boundaries. In addition, we find that the maximum *d*-wave amplitude in the sample is roughly 0.91 in the presence of the impurities, which should be compared to 1 in the absence of the impurities. The maximum magnitude of the superfluid current (not shown here) has also been reduced to roughly one-third of the intrinsic depairing current.

In principle, one could also obtain the current-voltage characteristics of a disordered superconductor. However, since there are many channels for the vortices to move along in a specific realization of the disorders, the dynamics depends on the initial configuration of the vortices. To mimic the bulk property, one would have to perform ensemble average over the realizations of the disorders. We shall not go into these complications here, but merely present in Fig. 7 the transport current dependence of the resistivity with respect to the realization in Fig. 6(d) in order to have a rough

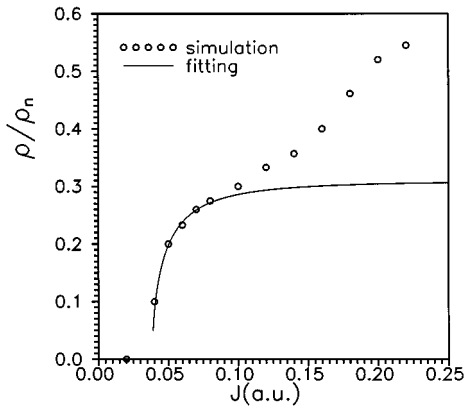

FIG. 7. The current dependence of the flux-flow resistivity. The solid line represents a fitting at low J.

idea of the depinning current for the vortex motion. The solid line in Fig. 7 is a fitting for the low current resistivity, $\rho/\rho_n = 0.31\sqrt{1-(0.0385/J)^2}$, yielding a depinning current $J_c = 0.0385$. (Note that the periodic boundary condition we applied justifies this fitting.) The quality of the fitting for low currents indicates that an effective overdamped particle model for vortex motion is still plausible. However, the asymptotic resistivity $(0.31\rho_n)$ is again significantly larger than the corresponding FFF resistivity, and the depinning current turns out to be drastically smaller than that in Fig. 5(b). The simulation data at larger current in Fig. 7 deviate quickly from the fitting curve, and can also be attributed to the same fact as in Fig. 5(b), namely, that the current is comparable with the maximum supercurrent around the vortex in the absence of the driving current. Clearly, the impurities in Fig. 6(d) are less efficient than the twin boundary in Fig. 5 as far as the pinning effect for vortex motion is concerned. A more comprehensive study on the pinning effect of disorders as a function of impurity density as well as the magnetic field in a *d*-wave superconductor awaits.

IV. SUMMARY

The time-dependent unconventional GL equations are analyzed by the finite-element method. The developed numerical method is flexible to deal with both open and periodic boundary systems in equilibrium as well as dynamical states in the presence of various types of disorders in *d*-wave superconductors. Simulation results of the single vortex and vortex lattice in bulk and finite-size samples are presented. The FFF resistivity and the flux-flow resistivity in the presence of a twin boundary or random impurities are discussed. The low-field FFF resistivity turns out to obey the law of corresponding states discovered in conventional superconductors, while the high-field resistivity reveals a noticeable effect of the *s*-wave coupling on lifting the effective upper critical field. The flux flow near and above the depinning current in the presence of a twin boundary or random impurities also assumes a conventional behavior, indicating that a model of overdamped particles subject to driving and pinning forces is still applicable. However, our results raise some doubts about the application of such a model since the asymptotic resistivity is almost one order of magnitude larger than the corresponding FFF resistivity in superconductors without disorders.

ACKNOWLEDGMENTS

We are grateful to Professor Qiang Du for helpful discussions on the finite-element method. This work is supported by a RGC grant of Hong Kong, and the Natural Science Foundation of China.

[1] D. A. Wollman, D. J. Van Harlingen, W. C. Lee, D. M. Ginsberg, and A. J. Leggett, Phys. Rev. Lett. **71**, 2134 (1993).
[2] C. C. Tsuei *et al.*, Phys. Rev. Lett. **73**, 593 (1994); J. H. Miller, Jr. *et al.*, *ibid.* **74**, 2347 (1995).
[3] A. G. Sun *et al.*, Phys. Rev. Lett. **72**, 2267 (1994).
[4] P. Chaudhari and S.-Y. Lin, Phys. Rev. Lett. **72**, 1084 (1994).
[5] P. Monthoux, A. V. Balatsky, and D. Pines, Phys. Rev. Lett. **67**, 3448 (1991).
[6] R. Combescot and X. Leyronas, Phys. Rev. Lett. **75**, 3732 (1995).
[7] G. E. Volovik, Pis'ma Zh. Eksp. Teor. Fiz. **58**, 457 (1993) [JETP Lett. **58**, 469 (1993)].
[8] K. A. Moler *et al.*, Phys. Rev. Lett. **73**, 2744 (1994).
[9] P. I. Soininen, C. Kallin, and A. J. Berlinsky, Phys. Rev. B **50**, 13 883 (1994).
[10] Y. Ren, J. H. Xu, and C. S. Ting, Phys. Rev. Lett **74**, 3680 (1995); J. Phys. Chem. Solids **56**, 1749 (1995).
[11] J. H. Xu, Y. Ren, and C. S. Ting, Phys. Rev. B **53**, R2991 (1996).
[12] A. J. Berlinsky, A. L. Fetter, M. Franz, C. Kallin, and P. I. Soininen, Phys. Rev. Lett. **75**, 2200 (1995).
[13] Q. H. Wang and Z. D. Wang, Phys. Rev. B **54**, R15 645 (1996).
[14] H. Won and K. Maki, Europhys. Lett. **30**, 421 (1995); N. Schopohl and K. Maki, Phys. Rev. B **52**, 490 (1995); H. Won and K. Maki, *ibid.* **53**, 5927 (1996).
[15] B. Keimer *et al.*, J. Appl. Phys. **76**, 6788 (1994); B. Keimer *et al.*, Phys. Rev. Lett. **73**, 3459 (1994); I. Maggio-Aprile, C. Renner, A. Erb, E. Walker, and Ø. Fisher, *ibid.* **75**, 2754 (1995).
[16] L. P. Gor'kov, Zh. Eksp. Teor. Fiz. **36**, 1918 (1959) [Sov. Phys. JETP **9**, 1364 (1960)].
[17] Z. D. Wang and C. R. Hu, Phys. Rev. B **44**, 11 918 (1991).
[18] Q. Du, M. D. Gunzburger, and J. S. Peterson, Phys. Rev. B **51**, 16 194 (1995).
[19] D. S. Burnett, *Finite Element Analysis: from Concepts to Applications* (Addison-Wesley, New York, 1987).
[20] In our case $J_{c0} = cH_c/3\sqrt{6}\pi\lambda$ with $H_c = \Phi_0/2\pi\sqrt{2}\xi\lambda$ (Ref. 23). In our dimensionless units, $J_{c0} = 0.3849$.
[21] C. F. Hempstead and Y. B. Kim, Phys. Rev. Lett. **12**, 145 (1964); A. R. Strnad, C. F. Hempstead, and Y. B. Kim, *ibid.* **13**, 794 (1964); Y. B. Kim, C. F. Hempstead, and A. Strnad, Phys. Rev. **139**, A1163 (1965); Z. D. Wang, Q. Wang, and P. C. W. Fung, Supercond. Sci. Technol. **9**, 333 (1996).
[22] Z. D. Wang, E. M. Y. Kwok, and P. C. W. Fung, Z. Phys. B **96**, 25 (1994).
[23] M. Tinkham, *Introduction to Superconductivity* (McGraw-Hill, New York, 1996).